

TABLE OF CONTENTS

Acknowledgements	iii
Abstract in English	vii
Abstract in Thai	ix
List of Tables	xvii
List of Figures	xviii
Chapter 1 Introduction	1
1.1 Femtosecond Electron Pulses as a Source of FIR Radiation	2
1.2 Femtosecond Electron Pulses as a Source of Femtosecond X-ray	5
1.3 Generation of Femtosecond Electron Bunches at SURIYA Facility	5
1.4 Overview of Thesis	9
Chapter 2 RF Principles and Creation of Electron Beam	11
2.1 Electromagnetic Waves and Resonant Cavity	11
2.1.1 Waveguide Principle	12
2.1.2 Resonant Cavity	15
2.2 RF Cavity Parameters	18
2.2.1 Resonant Frequency and Cavity Radius	18
2.2.2 Energy Gain in RF-cavity and Transit Time Factor	19
2.2.3 Accelerating Voltage and Accelerating Fields	19
2.2.4 Length of Cavity	20
2.2.5 Cavity Wall Losses and Shunt Impedance	20

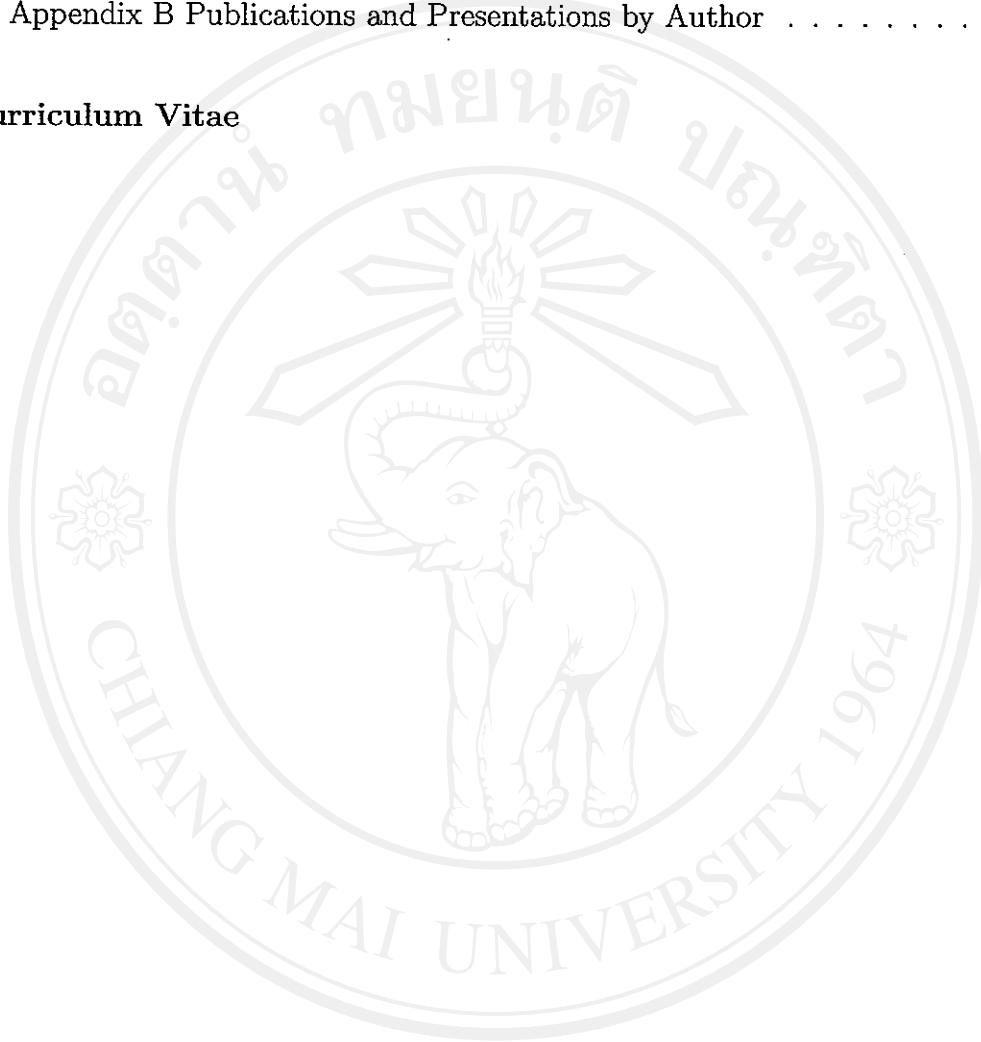
2.2.6	Quality Factor	22
2.2.7	Resonant Cavity and Equivalent Circuit	24
2.3	RF Coupling to Resonant Cavity	25
2.3.1	RF Coupling from RF-Generator to Resonant System . . .	26
2.3.2	RF Coupling Coefficient	26
2.3.3	Transient-Time Behavior	27
2.3.4	Voltage Standing Wave Ratio (<i>VSWR</i>)	28
2.4	Creation of Electron Beam	28
2.4.1	Electron Sources	28
2.4.2	Richardson-Dushman's Law	33
2.4.3	Schottky's Effect	34
2.4.4	Space Charge Effect and Child-Langmuir's Law	34
2.5	Time Structure and Beam Current Definitions	36
2.5.1	Beam Current from Ohm's Law	36
2.5.2	Peak Current	36
2.5.3	Pulse Current	37
2.5.4	Average Current	37
Chapter 3 RF-Gun Design and Beam Dynamic Study		39
3.1	Introduction	39
3.1.1	RF-Gun Characteristics	39
3.1.2	RF-Gun Numerical Simulations	41
3.1.3	Comparison of Analytical and SUPERFISH Calculations .	42
3.2	RF-Simulations	43
3.3	Beam Dynamic Study	45
3.3.1	Numerical Beam Simulations of RF-Gun	46

3.3.2	Bunch Compression	47
3.3.3	RF-Gun Field	49
3.3.4	Longitudinal Travel Time Formation	50
3.3.5	Ideal Phase Space Distribution	52
3.3.6	Beam Dynamic Simulations at Experimental Station	55
3.4	Transverse Particle Dynamics of RF-Gun	57
3.4.1	Effect of Cathode Size	60
3.4.2	Beam Emittance and Particle Energy	61
3.4.3	Schottky Effect	61
3.5	Parameters and Beam Dynamic Results for SURIYA RF-Gun	63
3.6	RF-Power Requirements	64
3.6.1	Cavity Wall Losses	65
3.6.2	Beam Power	66
Chapter 4	RF-Gun Construction and RF-Measurements	67
4.1	Introduction	67
4.2	SURIYA RF-Gun Construction	67
4.2.1	RF-Gun Component Forming	68
4.2.2	Vacuum Considerations	70
4.3	Thermionic Cathode Installation and Testing	72
4.3.1	Cathode Characteristics	72
4.3.2	Cathode Handling and Vacuum Concern	75
4.3.3	Cathode Processing	76
4.4	RF-Measurement Instrument and Methods	79
4.4.1	Network Analyzer and Scattering Parameters	79
4.4.2	Transmission Measurement	81

4.4.3	Reflection Measurement	82
4.5	RF Measurement of SURIYA RF-Gun	85
4.5.1	Resonant Frequency Measurements	85
4.5.2	Effect of Temperature and Vacuum Condition in RF-Cavity	88
4.5.3	Quality Factor and RF-Coupling Coefficient Measurement	91
4.5.4	On-axis Field Profile Measurement	93
4.5.5	Conclusion of RF Characterization of SURIYA RF-Gun	97
Chapter 5	SURIYA System and Diagnostic Instruments	99
5.1	Introduction	99
5.2	Magnetic bunch Compressor	101
5.3	Linear Accelerator	103
5.4	Focusing and Beam Steering Elements	104
5.5	RF Power System	106
5.5.1	Low-Level RF-System	107
5.5.2	RF-Amplify in Klystron	108
5.5.3	RF-Power Transmission to Accelerator	109
5.5.4	How to Measure RF-Power	110
5.6	Beam Diagnostic Instruments	111
5.6.1	Current Monitor	111
5.6.2	Beam Viewer Set Up	112
5.6.3	Dipole Magnet as Beam Dump and Energy Spectrometer	114
Chapter 6	Electron Beam Generation and Experimental Results	117
6.1	Introduction	117
6.2	RF-Gun Setup and Conditioning	117
6.2.1	Gun Temperature Control	117

6.2.2	Vacuum Baking	118
6.2.3	RF-Gun Conditioning and Breakdown Phenomena	119
6.3	RF-Gun Operation	121
6.3.1	Choice of RF-Power	122
6.3.2	Forward, Reflected and Absorbed RF-Power	123
6.4	RF-Gun and Electron Beam Characterization	126
6.4.1	Electron Beam Generation	126
6.4.2	Beam Loading and Electron Back Bombardment	128
6.4.3	Cathode Temperature Effect	129
6.4.4	Beam Current and Energy	132
6.4.5	Beam Profile Measurements	133
6.5	Electron Beam Acceleration from Linear Accelerator	135
6.6	Conclusion of Electron Beam Characteristics at SURIYA	139
Chapter 7	Transition Radiation from Electron Bunches	141
7.1	Radiation from Electron Bunches	141
7.2	Transition Radiation	146
7.3	Transition Radiation Acceptance	149
7.4	Coherent Transition Radiation Spectrum	151
7.5	Transition Radiation Generation and Observation	152
Chapter 8	Further Developments	155
8.1	Electron Beam Stability	155
8.2	Beam Transportation through the Linac	155
8.3	Bunch Length Measurement	156
	References	157

Appendices	162
Appendix A Geometry of RF-Gun	163
Appendix B Publications and Presentations by Author	165
Curriculum Vitae	167



ลิขสิทธิ์มหาวิทยาลัยเชียงใหม่
 Copyright© by Chiang Mai University
 All rights reserved

LIST OF TABLES

Table	Page
3.1 RF-parameters for a pillbox cavity from analytical and SUPERFISH calculations.	43
3.2 RF-parameters for the optimized RF-gun cavities from SUPERFISH simulations.	45
3.3 Optimized beam line lattice.	56
3.4 Optimized S-band RF-gun and beam parameters.	58
3.5 RF-parameters for the actual RF-gun cavities from SUPERFISH simulations.	63
3.6 Beam parameters of SURIYA RF-gun with the beam line in Fig. 3.9.	64
3.7 Beam line lattice for SURIYA system.	65
4.1 Thermionic tungsten dispenser cathode information [44][46].	73
4.2 Hastelloy C-276 properties [46].	74
4.3 Resonant frequency of the RF-gun at various operating temperature (in vacuum).	91
4.4 Electric field ratios of the full-cell to the half-cell by adjusting the tuning rod position.	96
4.5 RF-parameters of the RF-gun calculated using SUPERFISH comparing to the RF-measurement results for the actual gun dimensions. . .	97
5.1 Some parameters for the quadrupole magnets using at SURIYA system.	104
6.1 Electron beam parameters at different cathode heating powers.	132
6.2 Typical operating parameters and electron beam characteristics at SURIYA facility (April 2006).	139

LIST OF FIGURES

Figure		Page
1.1	Calculated radiation brightness B (ph/s/mm ² /100%BW) vs. wave number for CTR, SR, and BB.	4
1.2	Coherent transition raw-spectrum (dashed-line) and the corrected spectrum (solid-line) after applying the correction for beam splitter (BS) efficiency. The dotted-section occupy region near singularities of the BS efficiency [18].	4
1.3	Schematic diagram of SURIYA system, which consists of the S-band RF-gun, the α -magnet and the post linear accelerator.	6
1.4	Schematic diagram of SURIYA floor plan.	8
2.1	Infinite uniform circular metal waveguide.	12
2.2	Pillbox cavity of radius a and length d with electromagnetic field lines in the TM ₀₁₀ -mode.	16
2.3	Electric field as a function of radius a and length d of the TM ₀₁₀ -mode pillbox cavity.	17
2.4	Equivalent RLC circuit for a resonant cavity.	24
2.5	A schematic diagram of a simple Thermionic DC electron gun showing the cathode, the anode and the accelerating voltage V	30
2.6	Thermionic emission regimes and space charged limited.	35
2.7	Time structure (schematic) of electron bunches and pulses.	36
3.1	Cross-section and 3D-view of the SURIYA RF-gun.	40
3.2	Internal RF-gun geometry and the electric field lines.	44
3.3	Axial electric field profile inside the RF-gun.	45
3.4	Particle distribution in energy-time phase space for a single S-band bunch at the RF-gun exit with histogram. The units of the histogram are macroparticles (each representing 6.34×10^4 electrons) per picosecond.	46
3.5	RF-gun and α -magnet schematic layout.	48

3.6	Particle distribution in energy-time phase space after the bunch compression in the α -magnet.	49
3.7	Particle distribution in energy-time phase space for different accelerating fields in the RF-gun.	50
3.8	Comparison between longitudinal phase space distribution at the RF-gun exit (left curve) and at the experimental station (right curve). . .	53
3.9	Beam transport line from RF-gun to experimental station (QF1-QD1-QF2- α magnet-QF3-QD2-linac-QF4QD3). (Note: α -magnet is shown as a thin element.)	54
3.10	Ideal distribution and particle distribution from PARMELA simulation at the RF-gun exit.	54
3.11	Axial electric field profile for optimum accelerating field ratio in the half-cell and the full-cell.	55
3.12	Particle energy-time phase space distribution after bunch compression and transport to the experimental station with histogram. The histogram can be fitted by a Gaussian with a standard width of 53 fs and a charge of 94 pCb.	57
3.13	Transverse phase-space distribution at the exit of the SUNSHINE RF-gun (without space charge effects).	58
3.14	Transverse phase-space distribution of optimized RF-gun without (left) and with (right) space charge effects.	59
3.15	Transverse phase-space distribution of optimized RF-gun without (left) and with (right) space charge effects.	61
3.16	Relation of current density and time from Richardson's law with Schottky's correction.	62
4.1	Three-dimensional and cross-section view of the SURIYA RF-gun. . .	68
4.2	RF-gun parts after machining process.	69
4.3	Completed RF-gun after high temperature brazing process.	70
4.4	RF-gun baking diagram performing at SSRL vacuum laboratory in August 2002.	71

4.5	Assembly drawing of SURIYA cathode showing dispenser cathode, cathode plate, cathode holder and the end flange of the RF-gun. . . .	74
4.6	(a).Cathode holder and cathode heat-dam with toroidal-spring and (b). the cathode after mounted on the cathode plate.	75
4.7	Pyrometric measurement results show the cathode temperature as a function of the filament power for a brand new cathode, July 2005 (left) and for the present cathode of SURIYA RF-gun, March 2006 (right) .	78
4.8	RF-gun drawing and cross-section represented as a two-port RF device.	80
4.9	Two-port S-parameter Network Analyzer diagram.	81
4.10	Smith Chart representation for three degrees of coupling of RF-system.	83
4.11	Identification of the half-power points from the Smith Chart representation showing seven frequencies ($f_0, f_1, f_2, f_3, f_4, f_5$ and f_6). Q_0 locus is given by $x = r$, Q_L by $x = r \pm 1$ and Q_{ext} by $x = \pm 1$ [31].	84
4.12	RF-measurement setup at SSRL.	86
4.13	Schematic diagram of the side-coupling cavity and the tuning rod at position all the way in to close the coupling hole (left) and at the desired coupling position (right).	87
4.14	Smith Chart representation shows the resonant frequency and six frequencies f_1, f_2, f_3, f_4, f_5 and f_6 measuring for the SURIYA RF-gun.	92
4.15	Measured $VSWR$ signal from SURIYA RF-gun in low-power RF-measurement.	92
4.16	Schematic diagram of the bead-pull setup.	95
4.17	Longitudinal electric field distribution from bead-pull measurement when adjusting the tuning rod position. The tuning rod position in theses measurements are 10, 6, 4 and 2 mm (from top to bottom distribution).	96
4.18	Comparison of the longitudinal electric field distribution on axial axial from SUPERFISH and PARMELA simulations with bead-pull measurement.	97
5.1	Top view and side view drawings of SURIYA beam transport system.	100

5.2	The α -magnet field gradients as a function of the excitation current. .	102
5.3	Particle trajectories inside the α -magnet with the energy slits [41]. . .	102
5.4	Schematic diagram of square-frame steering magnet with its fields. The horizontal magnetic fields B_x (solid lines) deflect electron in ver- tical direction and the vertical magnetic fields B_y (dash lines) deflect electron on horizontal direction.	105
5.5	Schematic diagram of a small air coil dipole steering magnet with its fields.	106
5.6	Schematic layout of SURIYA RF-system.	106
5.7	Low-level RF system consisting of the RF-oscillator, the 90° hybrid directional coupler and the adjustable phase shifter.	107
5.8	Schematic picture illustrates the main components of the klystron tube [57].	109
5.9	Schematic model of current transformer (left) [55] and actual current transformer using at SURIYA (right) with a metallic shield taken off. .	112
5.10	Schematic layout of beam profile measurement set up [55].	113
5.11	3D-view of dipole magnet (left) and 3D-measured magnetic field map for the dipole magnet (right).	114
5.12	Design drawing of the vacuum chamber of the dipole magnet, the view screen set up and the Faraday cup.	115
5.13	Measured Maximum magnetic field in the dipole magnet as a function of excitation current(left) and calculated energy of the electrons as a function of the excitation current of the dipole magnet (right).	116
6.1	Forward (solid-line), reflected (dashed-line) RF-signals and the dark current (dots) with cathode heater off at 3.65 MW with $2\ \mu\text{s}$ (FWHM) RF-pulse width	120
6.2	Comparison of the RF-pulse with $6\ \mu\text{s}$ (solid-line) and $2.8\ \mu\text{s}$ (dashed- line) FWHM pulse length. The RF-power measurements were per- formed at $27.5\ ^\circ\text{C}$	123

6.3	Measured forward (solid-line) and reflected (dashed-line) RF-power from the RF-gun for the matched temperature at 27.5°C.	125
6.4	Measured forward (solid-line) and reflected (dashed-line) RF-power from the RF-gun at the off-resonance gun temperature at 35°C.	125
6.5	Waveforms of the forward (dashed-line), reflected (solid-line) RF-pulses and the typical electron pulses at the RF-gun (bottom curve). These waveforms were observed when the cathode power is 13.62 W ($\sim 950^\circ\text{C}$).	127
6.6	Normalized electron charge from the RF-gun as function of cathode temperature for different RF-power levels.	129
6.7	Maximum kinetic energy (black triangle) of electron beam and the beam pulse width (white triangle) as a function of cathode heating power.	131
6.8	Beam peak current (black dots) and the beam pulse width (white circles) as a function of cathode heating power.	131
6.9	RF-pulses and electron pulse currents (left) and energy spectrum (right) when the cathode heater power of 13.41 W (945°C).	133
6.10	RF-pulses and electron pulse currents (left) and energy spectrum (right) when the cathode heater power of 13.62 W (950°C).	134
6.11	RF-pulses and electron pulse currents (left) and energy spectrum (right) when the cathode heater power of 13.79 W (960°C).	134
6.12	2.4 MeV electron beam image (left), the relative intensity distribution of electron beam in two and three dimension and the horizon and vertical beam profiles.	135
6.13	Waveforms of the forward (bottom curve), reflected (top curve) RF-pulses of the linac at typical linac operation at 45°C	136
6.14	Beam pulse current measured at CT2 after bunch compression (dash line) and at CT3 after the linac acceleration (solid line).	138
7.1	Schematic model of an electron bunch of N electrons showing the coordinate of the j^{th} electron referring to the center of the bunch (C) and the observation point (O).	141

7.2	Schematic model of the radiation from short electron bunch (top) and long electron bunch (bottom) compared to the radiation wavelength.	144
7.3	Typical bunch distributions: (a). a uniform distribution with rectangular longitudinal distribution of length $2\sigma_z$ and (b). a Gaussian distribution with the FWHM of length $\sqrt{2\pi}\sigma_z$.	146
7.4	The two-charged-particle collision problem represents the transition radiation (dashed-arrow) emitted when an electron moves from vacuum to a perfect conductor in a direction normal to the interface [18].	147
7.5	An electron moves from vacuum to a perfect conductor in at an incident angle ψ with respect to the z -axis.	148
7.6	Radiation brightness B (ph/s/mm ² /100%BW) vs. wave number for coherent transition radiation for 16 μm and 35 μm compared to synchrotron radiation and black body radiation.	151
7.7	Transition radiation measurement setup.	152
7.8	The transition radiation (TR) signal at SURIYA facility (March 21, 2006). The top curve shows the TR signal observed with the pyroelectric detector and the bottom curve shows the TR signal when an Al-foil is placed between the source and the detector.	153